Aerodynamics and Far-field Noise Emissions of a Propeller in Positive and Negative Thrust Regimes at Non-zero Angles of Attack

AIAA AVIATION Forum
12-16 June 2023, San Diego, CA and Online
AIAA AVIATION 2023 Forum

10.2514/6.2023-3217

Aerodynamics and Far-field Noise Emissions of a Propeller in Positive and Negative Thrust Regimes at Non-zero Angles of Attack

Jatinder Goyal*, Tomas Sinnige†, and Carlos Ferreira‡
Delft University of Technology, Delft, 2629 HS, Netherlands

Francesco Avallone§
Politecnico di Torino, Torino, 10129, Italy

This paper studies the effect of operation at non-zero angles of attack on the aerodynamic performance and far-field noise emissions of an isolated propeller operating at positive and negative thrust conditions. To achieve this, scale-resolved lattice-Boltzmann very large eddy simulations coupled with the Ffowcs Williams & Hawkings analogy have been used. The results show that when the propeller operates with a 10° angle of attack at the positive thrust condition, the blade loading increases on the advancing side and decreases on the retreating side, leading to a 9.6% increase in integrated thrust (when computed along the propeller axis) and a negligible increase (0.1%) in propeller efficiency. Conversely, at the negative thrust condition, the operation at 10 deg angle of attack results in a 7.9% decrease in thrust magnitude and an 11.1% reduction in energy-harvesting efficiency. In this condition, the positively cambered blade sections exhibit dynamic stall at the 10° angle of attack, resulting in broadband fluctuations of up to 10% of the mean loading. As a result of the opposite change in absolute blade loading in the negative thrust condition compared to the positive thrust condition at the 10° angle of attack, the change in the noise directivity is also the opposite. Whereas in the positive thrust case, the noise increases in the region from which the propeller is tilted away (i.e., below the propeller at a positive angle of attack), in the negative thrust case, it is the other way around. This study highlights the need to account for non-zero angles of attack in propeller design and optimization analyses.

Nomenclature

B	number of propeller blades	c	section chord, m
BPF	$B \cdot n$, blade passing frequency, Hz	c_o	speed of sound in dry air at 15° C, m/s

*PhD candidate, Wind Energy Section, Faculty of Aerospace Engineering, Kluyverweg 1; J.Goyal@tudelft.nl.
†Assistant professor, Flight Performance and Propulsion Section, Faculty of Aerospace Engineering, Kluyverweg 1; T.Sinnige@tudelft.nl. Member AIAA.
‡Full professor, Wind Energy Section, Faculty of Aerospace Engineering, Kluyverweg 1; C.J.SimaoFerreira@tudelft.nl. Member AIAA.
§Assistant professor, Department of Mechanical and Aerospace Engineering, Corso Duca degli Abruzzi 24; francesco.avallone@polito.it.

C_l sectional lift coefficient

C_P $P/\rho_\infty n^3 D_\mathrm{p}^5$, propeller power coefficient

c_p $\frac{p - p_\infty}{0.5\rho_\infty((V_\infty \cos\alpha_\infty)^2 + (\Omega r + V_\infty \sin\alpha_\infty \sin\phi)^2)}$, sectional pressure coefficient based on local dynamic pressure

C_T $T/\rho_\infty n^2 D_\mathrm{p}^4$, propeller thrust coefficient

D propeller diameter, m

f frequency, Hz

F_N Force in the normal direction (Z-Axis), N

F_Y Force in the side direction (Y-Axis), N

J V_∞/nD_p, propeller advance ratio

$\Delta J'$ $V_\infty \cos\alpha_\infty/(n + \frac{V_\infty \sin\alpha_\infty \sin\phi}{2\pi r})D_\mathrm{p}$, change in effective advance ratio

M_ht $\sqrt{M_\infty^2 + M_\mathrm{tip}^2}$, helicoidal tip rotational Mach number

M_tip $\Omega R/c_\mathrm{o}$, tip rotational Mach number

M_∞ Freestream Mach number

n propeller rotation speed, Hz

N_C $F_N/\rho_\infty V_\infty^2 D_\mathrm{p}^2$, Normal force coefficient based on freestream dynamic pressure

OSPL overall sound pressure level, dB

P propeller power, W

p static pressure, Pa

PSD power spectrum density, dB/Hz

p_ref reference sound pressure, Pa

P_C $P/\rho_\infty V_\infty^3 D_\mathrm{p}^2$, propeller power coefficient based on freestream dynamic pressure

R propeller radius, m

r radial coordinate, m

Re_c Reynolds number based on chord of the propeller blade

T propeller thrust, N

t section thickness, m

T'_C $T'/\rho_\infty V_\infty^2 D_\mathrm{p}$, sectional thrust coefficient based on freestream dynamic pressure

T_C $T/\rho_\infty V_\infty^2 D_\mathrm{p}^2$, propeller thrust coefficient based on freestream dynamic pressure

V_∞ freestream velocity, m/s

X Axial coordinate, m

Y, Z Axes in the plane of propeller rotation, m

Y_C $F_Y/\rho_\infty V_\infty^2 D_\mathrm{p}^2$, Side force coefficient based on freestream dynamic pressure

Greek Symbols

α angle of attack, deg

$\beta_{0.7R}$ blade pitch angle at 70% of the radius, deg

$\Delta\phi$ $\tan^{-1}(Y_C/N_C)$, phase delay, deg

η_P TV_∞/P, propeller efficiency

η_t P/TV_∞, turbine efficiency

Ω $2\pi n$, rotational speed in rad/s

ϕ azimuthal position, deg

ρ air density, $\mathrm{kg/m^3}$

σ standard deviation

θ axial directivity angle, deg

Subscripts/Superscripts

$'$ per unit span

∞ freestream

I. Introduction

The increasing need for sustainable aviation has triggered the development of many new technologies. The use of fuel cells, hydrogen combustion, and electric architectures are a few examples of innovative technologies to store/deliver energy during flight. These technologies are generally coupled with open rotors to produce thrust and increase the

system's overall performance. Open rotors are preferred simply because of their high propulsive efficiency up to moderate Mach number and at low cruise altitudes [1]. These open rotors are expected to be driven by electric motors to make use of distributed propulsion along with tip-mounted configurations. One additional benefit of electric propulsion is that propellers can be operated at negative thrust settings that can be beneficial for achieving steeper descent, reduced landing run, better maneuverability [2, 3], reduced community noise [4], and regeneration of energy.

The concept of operation at negative thrust settings has already been implemented by Pipistrel, leading to 19% energy savings for a small electric trainer aircraft [5]. Only a few studies have focused on open rotors operating at negative thrust regimes. The previous work of the authors' [6] and the study by Nederlof et al. [7] focused on isolated propellers operating in uniform inflow conditions. However, the use of negative thrust could especially be interesting during the descent phase of the mission, in which the angle of attack of the propeller will be nonzero. Sinnige et al. [8] focused on the wing-tip mounted configuration and showed that the reduced dynamic pressure and reversed swirl in the propeller slipstream worsen the propeller-wing system lift and drag performance for inboard-up rotation. They showed that the system performance could be improved by using outboard-up rotation. Therefore, the performance change at the system level is known; however, the effect of installation on the propeller performance is still unknown. Such knowledge can help to optimize the propeller to maximize the aerodynamic performance and minimize acoustic emissions.

The installation effect on a propeller installed upstream or downstream of a wing can be alternatively estimated by the performance of the propeller operating at a non-zero angle of attack [9]. Therefore, this study is focused on the aerodynamic and aeroacoustic performance of the propeller operating at non-zero angles of attack in negative and positive thrust regimes. For this purpose, lattice-Boltzmann (LB) very large-eddy simulations (VLES) have been carried out. This method has the advantage of low dispersion and dissipation [10, 11], and lower computation cost compared to Navier-Stokes (NS) based solver, making it suitable for studying complex flowfields, as expected in this problem. The solver is coupled with the Ffwocs Williams and Hawkings (FWH) integral solution based on Farassat's formulation 1A [12] for aeroacoustic investigation. This paper analyzes the changes in the integrated propeller performance, blade loading, and loading fluctuations to understand the differences between the propeller performance in the positive and negative thrust regimes. The far-field noise has been computed over two rings around the propeller, and the changes in the noise emissions have been investigated.

II. Computational Setup

This section explains the detail of the LBM simulations and the numerical setup. It is followed by the rotor geometry and the operating conditions used for the validation of the setup.

A. Methodology

LBM simulations have been chosen for two main reasons. The first reason is its past proven record for similar applications [13, 14]. Secondly, the low dissipation and dispersion [10, 11] makes it suitable for aeroacoustic study. A detailed description of LBM can be found in refs. [15] and [16]. The simulations were performed using the latest version of the commercial solver PowerFLOW 6-2021 developed by 3DS Simulia, which was introduced in the reference paper [17]. This adopted version is especially suitable for the current application as it does not require a zig-zag trip to switch to the scale-resolving solver. Using a zig-zag trip can modify the flow separation and the broadband noise behavior [18, 19], which is not desired in this research.

The volume of the domain is discretized using a Cartesian mesh. In total, 19 discrete velocities are used in three dimensions (D3Q19), including a third-order truncation of the Chapman-Enskog expansion. An explicit time integration approach is used to solve the equations at the Courant-Friedrichs-Lewy (CFL) number of 1 for stability. The particle distribution is obtained using a collision term based on a unique Galilean invariant [20], and equilibrium distribution of Maxwell-Boltzmann [21]. A VLES model is implemented in PowerFLOW to take into account the effect of the subgrid unresolved scales of turbulence, which uses $k - \epsilon$ renormalization equations [22] to compute the turbulent relaxation time. The no-slip boundary condition on walls is approximated using a pressure-gradient extended wall model [23, 24].

A hybrid CFD/CAA approach has been used to compute the far-field noise to avoid excessive computational costs related to resolving the propagation of acoustic waves to the far field. The FWH analogy was solved based on the forward-time solution [25] of Farassat's formulation 1A [12] using the post-processing software SIMULIA PowerACOUSTICS. This so-called solid formulation includes surface integrals, i.e., acoustic monopoles (thickness noise) and dipoles (loading noise) terms. The volume integral, i.e., quadrupole term, is neglected because the propeller is operating at subsonic Mach numbers [26].

B. Computational Volume and Boundary Conditions

The computational domain is a cube with a domain size of $128D$ in all three directions (figure 1a). The boundary conditions were specified as a velocity inlet combined with a pressure outlet and slip walls. The propeller geometry was rotated around the Y-axis to change the angle of attack (instead of the inlet velocity) to keep the freestream aligned with the far-field slip walls. The no-slip condition was used for the propeller blades, spinner, and nacelle. For the sliding mesh, a volume of revolution was defined around the propeller blades and spinner. In the radial direction, a clearance of $0.1R$ was defined between the blade tip and the outer edge of the rotating domain. Similarly, in the axial direction, a clearance of $0.05R$ was defined between the spinner edge and the edge of the rotating domain.

In total, 13 variable resolution (VR) regions were used based on the ref. [27]. The cell volume changes by a factor of 8 between different VR regions. The finest three VR regions (VR13-11) were used around the propeller to accurately capture the flow around the propeller blades, as marked in figure 1b. VR10 was used in the sliding domain

and downstream of the sliding domain up to $0.5R$. Further downstream, VR10 is defined as a hollow cylinder to capture the strong gradients of tip vortices. VR9 was used in the cylinder encapsulating the propeller blades, spinner, and blade with a radius of $1.2R$ and extended $1R$ upstream and $3.5R$ downstream of the propeller. Other VR regions (1-8) were there to ensure that the domain was large enough to minimize any spurious acoustic reflections from the boundaries of the domain.

Further, an acoustic sponge was used to absorb any remaining acoustic reflections coming from the boundaries by exponentially varying the kinematic viscosity per unit temperature from 0.005 $m^2/(s.K)$ at $15R$ up to 0.5 $m^2/(s.K)$ at $30R$ as shown in figure 1a. As the acoustic sponge starts at a $15R$ distance from the propeller, its effect on the aerodynamic results is assumed to be minimal.

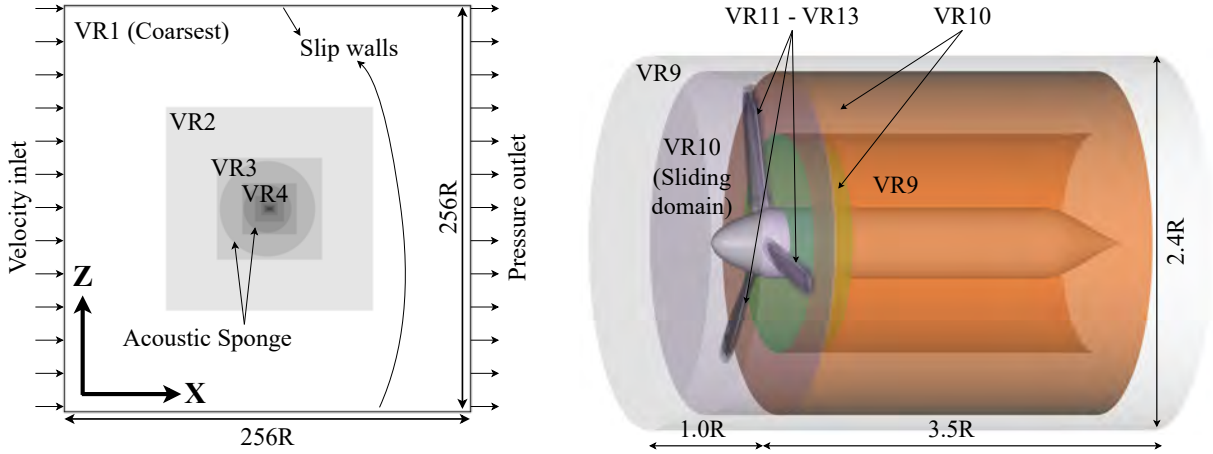

(a) Full computational domain

(b) Zoomed view of domain showing the distribution of VR regions near the propeller

Fig. 1 Computational domain and boundary conditions along with the VR regions

C. Rotor Geometry

The rotor used in this study is the TUD-XPROP, which is a scaled version of a propeller for a previous-generation regional turboprop aircraft. The rotor has a diameter of 0.4064 m and a hub diameter of 0.092 m. The nacelle of the rotor extended up to approximately $1.6D$ downstream. Originally, the propeller had six blades; however, only three blades were used for this study due to limitations of the experimental facility [7]. The propeller can be seen in figure 2a along with its geometry parameters in figure 2b.

D. Operating Conditions

The operating conditions were chosen based on the available experimental data for the validation of the numerical setup. Two angles of attack: 0° and 10°, have been chosen for validation and further analysis. The corresponding details of the operating conditions are listed in Table 1.

(a) Isolated propeller with three blades installed on a sting

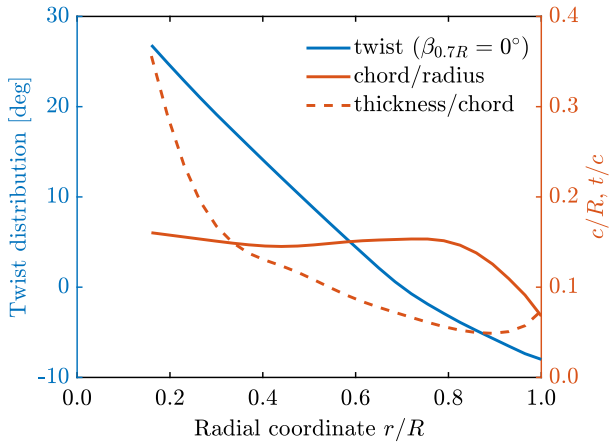

(b) Propeller blade geometry

Fig. 2 Propeller setup and geometry

Table 1 Operating conditions for the analysis

α_∞ [°]	$\beta_{0.7R}$ [°]	J	V_∞ [m/s]	n [Hz]	M_{ht}	max Re_c
0°, 10°	15°	0.60	30	123.03	0.47	3.5×10^5
0°, 10°	15°	1.10	30	67.11	0.27	2.0×10^5

The first advance ratio, i.e., $J = 0.60$, is the positive thrust condition with a moderate thrust. Though the given pitch angle is not optimal for propulsive operation and leads to separation near the trailing edge [6], it is still a useful reference for the changes in the positive thrust condition with the change in the angle of attack. The second condition is the negative thrust condition with $J = 1.10$ and is close to the maximum power output point at $\alpha_\infty = 0°$ as can be seen in refs. [6, 7].

E. Conventions

When the propeller operates at a non-zero angle of attack, the flow is no longer aligned with the propeller axis, resulting in an in-plane velocity component varying with the azimuthal position. Figure 3 shows the convention for the phase angle (ϕ) used to define the azimuthal position.

The blades on the downgoing side (i.e. the advancing side) experience an increase in the in-plane velocity component, while the opposite is observed on the upgoing blades (i.e. the retreating side). This leads to a reduction and an increase in the effective advance ratio for the advancing and retreating side, respectively, as depicted in figure 4. As the baseline advance ratio is higher for the negative thrust condition (1.10), the change in the local advance ratio due to the in-plane velocity component is also higher, as shown in figure 4b in comparison to figure 4a. The local inflow angle at each

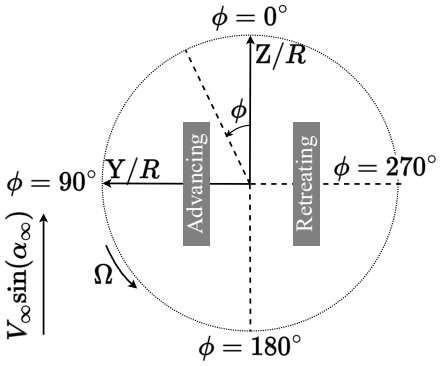

Fig. 3 Definition of phase angle (ϕ) and conventions used in this study

blade section is directly proportional to the local advance ratio. Therefore, for a given pitch angle and twist distribution, the local advance ratio has a direct impact on the local angle of attack at the blade sections. The more the advance ratio changes in a positive manner (figure 4), the greater the negative change in the local angle of attack (compared to a uniform inflow case). As a result, the most substantial positive change in the local angle of attack occurs at ϕ = 90° (i.e., the advancing side) near the propeller root. Similarly, the most significant negative change in the angle of attack occurs at ϕ = 270° (i.e., the retreating side).

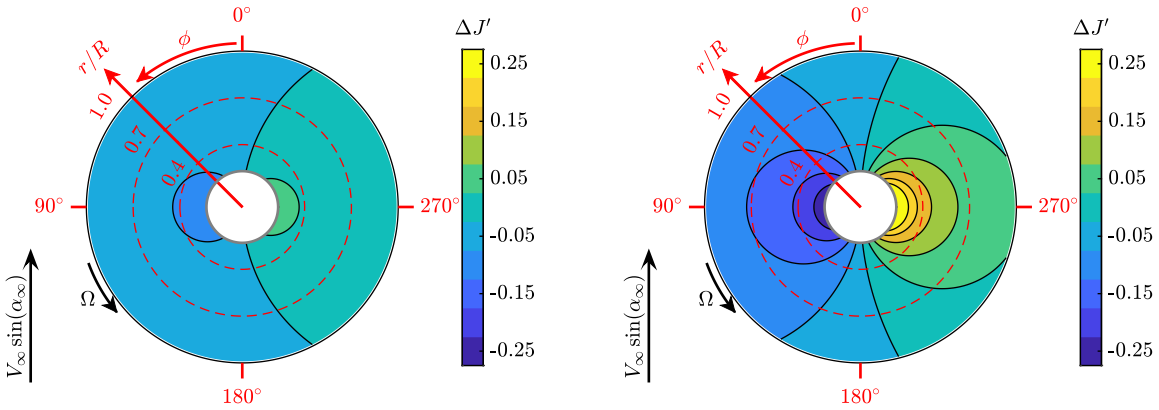

(a) Propulsive condition (J = 0.60) **(b) Regenerative condition (J = 1.10)**

Fig. 4 Change in the effective advance ratio over a rotation at 10° angle of attack compared to 0° angle of attack

The sinusoidal variation in the inflow conditions at non-zero angles of attack leads to a delayed aerodynamic response [9, 28]. This delay is denoted by $\Delta\phi$ and is described using equation 1. As the change in thrust and tangential forces on advancing and retreating sides is different, there is an in-plane force acting at $\Delta\phi$ with respect to the normal. Therefore, in addition to thrust and torque, a normal (N_C) and side force (Y_C) also acts on the shaft at non-zero angles

of attack.

$$\Delta\phi = \tan^{-1}\left(\frac{Y_C}{N_C}\right) \tag{1}$$

The change in the propeller performance along the propeller axis does not necessarily represent the changes in the performance along the freestream direction. The performance along the freestream direction is especially relevant for the performance of the system at the aircraft level. Therefore, two types of definitions have been used while comparing the propeller performance: 1) aligned with the propeller axis; 2) aligned with the freestream. The definitions of parameters aligned with freestream are given in the equations below:

$$T_{C_\infty} = T_C \cos\alpha_\infty - N_C \sin\alpha_\infty \tag{2}$$

$$\eta_{p_\infty} = \frac{T_{C_\infty}}{P_C} \tag{3}$$

$$N_{C_\infty} = N_C \cos\alpha_\infty + T_C \sin\alpha_\infty \tag{4}$$

III. Aerodynamic Results

The aerodynamic result section has been divided into two main subsections. Firstly, validation of the numerical setup has been done by comparing the integrated forces with the experimental data followed by the analysis of the blade loading.

A. Comparison of Propeller Shaft Forces with Experimental Data

The LBM simulations were validated using the unpublished data available from the experiments of Nederlof et al., part of which has been published in ref. [7]. The scatter in the experimental data at 0° made it necessary to compare the change in the forces with the angle of attack rather than the absolute values. Moreover, it allows the removal of any bias due to differences in prediction between experiments and simulations at 0° angle of attack itself. Upon subtracting the 0° values, the experimental data fall on a parabolic curve as can be seen in figure 5. The shaded regions show the minimum and maximum change in the thrust and power coefficients in the experiment over multiple acquisitions. The solid line with 'o' markers represents the experimental mean values, whereas the '+' markers represent LBM simulation data.

The LBM simulations can predict changes in the thrust and power coefficients but with some overprediction. Especially the change in the power coefficient for $J = 1.10$ (negative thrust condition) is noticeably larger in simulations than in the experiments. The overprediction is expected to be a result of the dynamic stall happening on the propeller blades over the rotation, which will be discussed in the paper at a later stage. As the reattachment location due to dynamic stall can be very difficult to mimic in the simulations, it can lead to overprediction of the power coefficient.

Nevertheless, the overprediction should not pose a problem for studying the changes in aerodynamic and aeroacoustic characteristics compared to the zero-degree angle of attack. Therefore, these LBM simulations have been considered suitable for understanding the changes in the blade loading and far-field noise characteristics in both positive and negative thrust regimes.

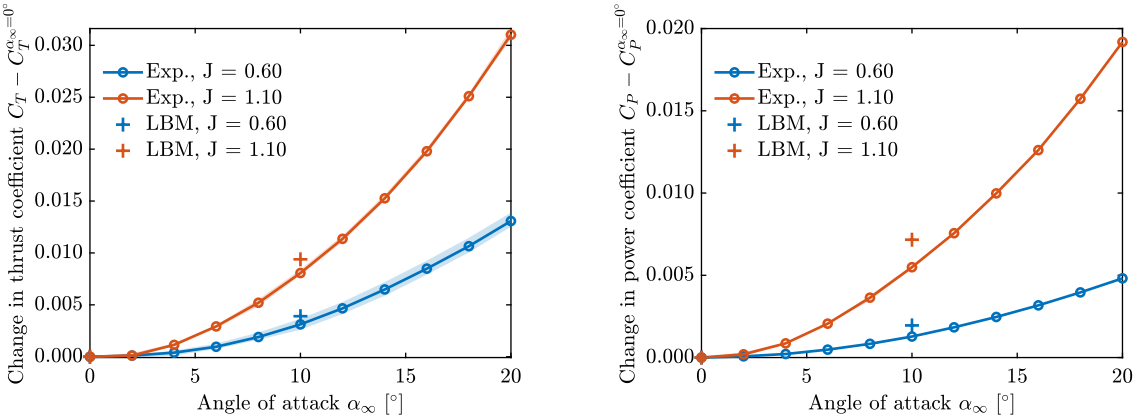

(a) Thrust coefficient **(b) Power coefficient**

Fig. 5 Comparison of simulated and experimental changes in integrated forces with the angle of attack variation

For the chosen operating conditions, the change in the angle of attack results in a significantly higher change in C_T and C_P for the negative thrust condition ($J = 1.10$) compared to the positive thrust condition ($J = 0.60$) as shown in figure 5. This is a result of the lower rotational speed at the higher advance ratio leading to higher coefficient values. Both thrust and power coefficients follow a positive parabolic trend irrespective of the thrust regime. Increasing the absolute angle of attack increases the magnitude of thrust and power in the positive thrust regime but decreases absolute thrust and power in the negative thrust regime.

Table 2 shows the simulated shaft forces at 0° and 10° angles of attack. In this table, T_C and P_C are used for the comparison instead of C_T and C_P. The former coefficients are based on the freestream velocity (30 m/s), making it easier to compare the two operating conditions.

Table 2 Forces on the propeller in positive and negative thrust conditions at 0° and 10° angles of attack

J	α_∞ [deg]	T_C	P_C	η_p	T_{C_∞}	η_{p_∞}	Y_C	N_C	N_{C_∞}	$\Delta\phi$ [deg]
0.60	0°	0.1135	0.1645	0.6898	0.1135	0.6898	0	0	0	–
	10°	0.1243	0.1736	0.7163	0.1198	0.6903	0.0043	0.0152	0.0365	15.7°
	Δ%	9.56%	5.50%	3.85%	5.58%	0.07%	–	–	–	–
J	α_∞ [deg]	T_C	P_C	η_t	T_{C_∞}	η_{t_∞}	Y_C	N_C	N_{C_∞}	$\Delta\phi$ [deg]
1.10	0°	-0.0985	-0.0483	0.4908	-0.0985	0.4908	0	0	0	–
	10°	-0.0907	-0.0430	0.4734	-0.0913	0.4705	0.0031	0.0112	-0.0047	15.5°
	Δ%	-7.88%	-11.14%	-3.54%	-7.30%	-4.14%	–	–	–	–

In the propulsive condition ($J = 0.60$), increasing the angle of attack from 0° to 10° results in a 9.56% increase in thrust and a 5.50% increase in power. This corresponds to a 5.58% increase in thrust along the freestream direction. The increase in thrust leads to a 3.85% increase in propeller efficiency (η_p) along the propeller axis. However, there is a negligible improvement in efficiency (η_{p_∞}) along the freestream direction due to the corresponding increase in power, as expected [29].

When the angle of attack is increased from 0° to 10° under the negative thrust condition ($J = 1.10$), the thrust and power along the propeller axis show a decrease of 7.88% and 11.14%, respectively. This is in contrast to the propulsive case. The thrust along the freestream direction is slightly higher than the thrust along the propeller axis. This can be attributed to the positive contribution from the normal force. However, the decrease in power is more substantial than the decrease in thrust, leading to a decrease in turbine efficiency by 3.54%.

In the positive thrust case, the side force coefficient (Y_C) and normal force coefficient (N_C) are 0.0043 and 0.0152, respectively, which indicate a $\Delta\phi$ of 15.7°. When calculated perpendicular to the freestream direction, this results in a normal force coefficient (N_{C_∞}) of 0.0365, indicating a positive lift generated by the propeller. In the negative thrust case, even though the direction of thrust and torque is reversed, the directions of normal and side force stay the same as in the positive thrust case. This results in a small negative lift, $N_{C_\infty} = -0.0047$. In both cases, the normal force coefficient (N_C) is about 12%, and the side force coefficient (Y_C) is about 3.5% of the thrust coefficient (T_C). The phase delay for both advance ratios is approximately 15°, which is in agreement with the typical value given by Van Arnhem [9]. Van Arnhem argues that the phase delay depends on the slenderness of the blades, and since the slenderness ratio does not significantly vary between modern propellers, a phase delay of around 15° can be expected.

B. Propeller Blade Loading

The effect of non-zero angle of attack on propeller performance is well established for the positive thrust conditions [9, 30, 31]. In positive thrust conditions, the decrease in the advance ratio on the advancing side leads to an increase in thrust, while the opposite effect is seen on the retreating side, as shown in figure 6a. However, the gradient of absolute thrust is reversed with the advance ratio in negative thrust conditions, resulting in the opposite trends observed in figure 6b. As the instantaneous data from the simulation is available from only eight rotations (due to computational costs), the averaging over time might not have converged, leading to the noise in contours in figure 6. Despite the noise, the results can still be used to understand the changes in the blade loading at non-zero angles of attack.

The region near the hub experiences the highest change in advance ratio due to the low rotational speed with respect to the axial inflow, as depicted in figure 4. However, the loading is relatively low in this region, resulting in a low absolute change in the thrust coefficient, as seen in figure 6. According to ref. [9], the radial locations with the maximum loading in the uniform inflow case are expected to show the highest absolute change in thrust. This holds true for the positive thrust case. However, in the negative thrust case, the absolute change in the thrust coefficient is relatively small

along the radial direction, see figure 6b.

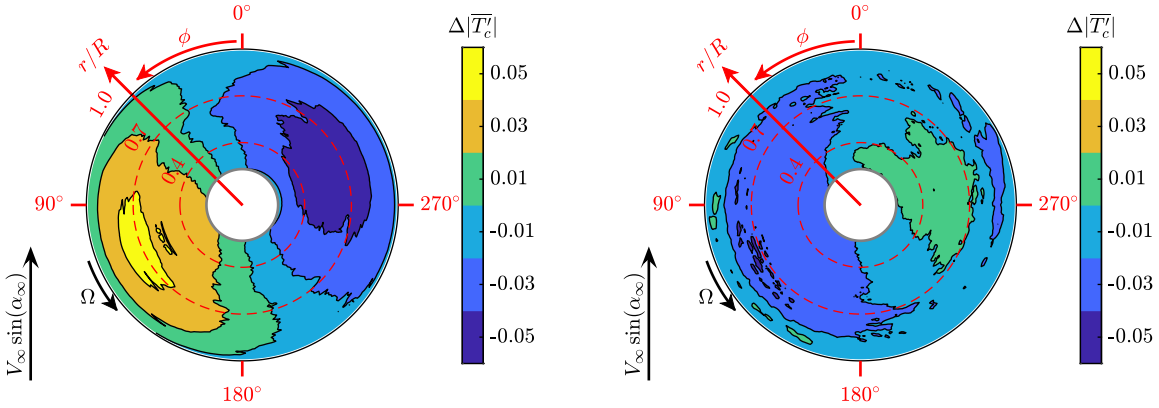

(a) Propulsive condition ($J = 0.60$) **(b) Regenerative condition ($J = 1.10$)**

Fig. 6 Change in time-averaged thrust distribution on the propeller blade operation at 10° angle of attack compared to 0° angle of attack case

The difference between the positive and negative thrust regimes can be attributed to the conventional propeller design featuring airfoils with positive camber. To gain a deeper insight into the aerodynamics of blade sections along the radial direction and how non-uniform inflow affects them, two blade sections have been chosen for analysis. These sections include the blade section located near the root at $r/R = 0.30$ and the section in the region of maximum loading at $r/R = 0.70$. The streamlines around these sections at different azimuthal positions, along with the contours of static pressure coefficient, are presented in figures 7 and 8 for the positive and negative thrust conditions, respectively.

In the case of uniform inflow at $J = 0.60$, the flow remains attached over the blades [6]. At $r/R = 0.30$ (figures 7e to 7h), the cross-flow component causes ±3° change in the angle of attack, while at $r/R = 0.70$ (figures 7a to 7d), the angle of attack changes by only 1.5° and −1° at $\phi = 90°$ and 270°, respectively, ignoring induction effects. As the angle of attack decreases from $\phi = 90°$ to 270°, the suction peak on the upper part of the airfoil decreases for both radial locations. Additionally, a small pressure peak develops at the leading edge on the lower part of the airfoil due to the geometrically negative angle of attack. As the angle of attack increases between $\phi = 270°$ to 90°, the pressure peak on the upper part increases again, and the suction peak on the lower part decreases. At $r/R = 0.30$, a separation bubble forms at $\phi = 270°$ (figure 7h), which is also present at $\phi = 0°$ (figure 7e). Despite having the same geometrical angle of attack for $\phi = 180°$ and 0°, the separation bubble is not observed at $\phi = 180°$ (figure 7g). The existence of this separation bubble at $\phi = 0°$ can be attributed to the delay in the aerodynamic response.

At $J = 1.10$, the cross-flow component results in a larger change in angle of attack compared to the $J = 0.60$ case. Specifically, at $r/R = 0.30$, there is a ±6° change in angle of attack, whereas at $r/R = 0.70$, the change is only 3° and −2° at $\phi = 90°$ and 270°, respectively, ignoring induction effects. At $\phi = 90°$, the flow remains attached at $r/R = 0.30$, but there is a large leading-edge separation bubble at $r/R = 0.70$, as shown in figures 8b and 8f. Previous study [6]

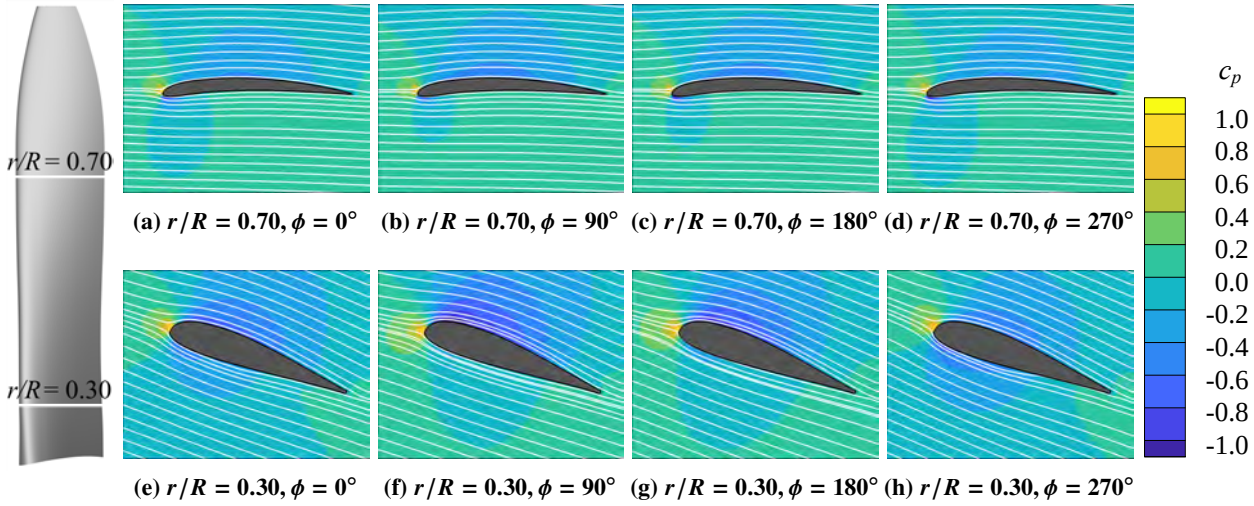

Fig. 7 Flow around blade sections at different radial locations (r/R) for the propulsive condition ($J = 0.60$) at 10° angle of attack

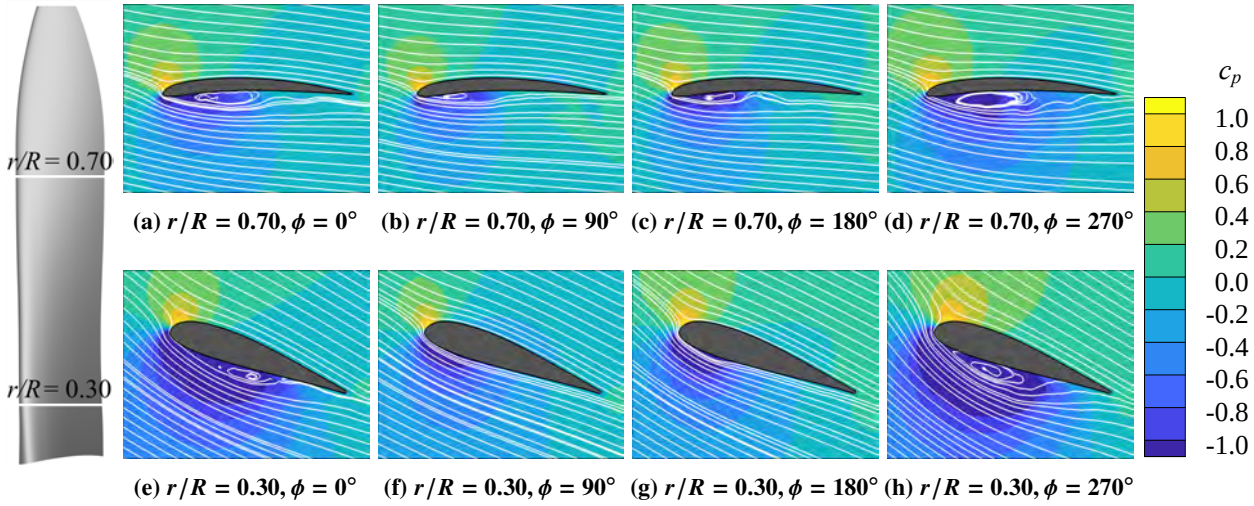

Fig. 8 Flow around blade sections at different radial locations (r/R) for the negative thrust condition ($J = 1.10$) at 10° angle of attack

for the uniform inflow reported that only a small inboard portion of the blade has attached flow. However, it can be observed from figure 8 that the blade sections exhibit dynamic stall at non-zero angles of attack. This can be observed in figures 8a to 8d for blade section $r/R = 0.70$.

As the angle of attack decreases (becoming increasingly negative), a separation bubble appears on the bottom side of the airfoil, which grows and extends up to the trailing edge at $\phi = 270°$ for $r/R = 0.70$ (figure 8d). As the blade continues to rotate, the angle of attack increases (decreasing in absolute terms). Notably, despite having the same geometrical angle of attack for $\phi = 180°$ and 0°, a larger separation bubble exists at $\phi = 0°$ compared to $\phi = 180°$ due to delayed aerodynamic response. A similar trend is observed for $r/R = 0.30$, where the separation bubble grows until $\phi = 270°$, after which it is reduced with an increase in the angle of attack.

1. Periodic and Broadband Fluctuations

When propeller blades operate in negative thrust conditions, the flow separation around them causes broadband fluctuations in blade loading, which act as sources of both noise and structural vibrations. Figure 9 displays the root mean square (RMS) of the broadband fluctuations of thrust over eight rotations, normalized with the absolute mean thrust, for $J = 1.10$. In the case of uniform inflow, it is evident from figure 9a that the fluctuations increase with radial location due to the increasing separation as observed in previous work [6]. For the inboard part of the blade, where the flow is attached, the fluctuations are nearly negligible up to $r/R = 0.50$. However, in the mid-board sections ($0.5 < r/R < 0.8$), the fluctuations are around 5% and increase up to 10% or even more at the blade tip.

The non-uniform inflow changes the distribution of broadband fluctuation over the blade; see figure 9b. As the inboard part of the blade exhibits dynamic stall (figure 8), during the part of the rotation ($\phi = 75° - 195°$) over which the flow is almost fully attached, fluctuations with negligible amplitude are observed. However, as the separation bubble extends to the trailing edge, it leads to fluctuations of up to 5%. Even on the outer part of the blade, the fluctuations are amplified on the retreating side and are comparatively reduced on the advancing side (as expected). Near the propeller tip, the fluctuations are less sensitive to changes in the angle of attack, as the flow is already separated there even at a 0° angle of attack.

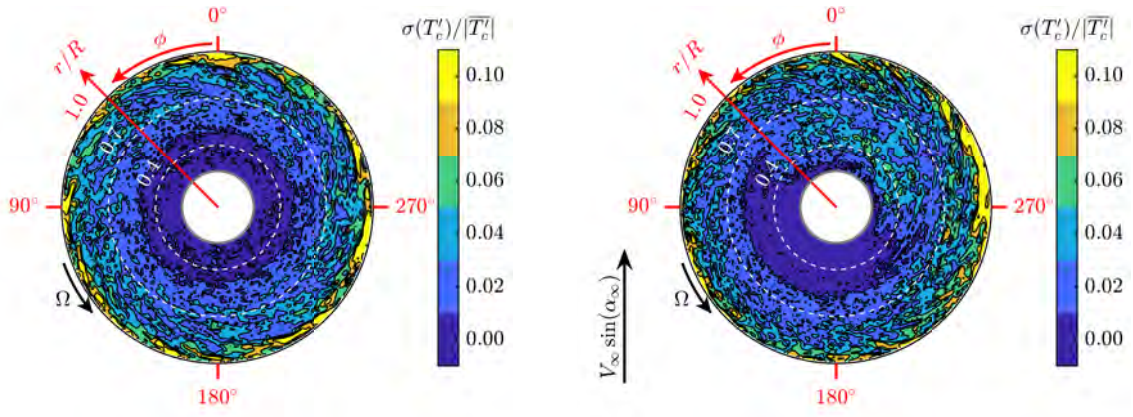

(a) $\alpha_\infty = 0°$ **(b) $\alpha_\infty = 10°$**

Fig. 9 RMS of broadband fluctuations in thrust distribution at 0° and 10° angle of attack for negative thrust condition ($J = 1.10$)

Given the increased broadband fluctuations in the negative thrust condition, it is important to compare the relative amplitude of the periodic and broadband fluctuations. For this purpose, the absolute mean value has been subtracted from the time-averaged thrust coefficient. The resulting quantity has been normalized with the absolute mean value to asses the periodic variation in the local thrust coefficient. The amplitude of broadband fluctuations has been indicated with the shaded regions showing the standard deviation of the quantity.

Figure 10 displays the periodic variations along with broadband fluctuations observed in local thrust coefficient at

three radial stations: $r/R = 0.30$, 0.70, and 0.90, which correspond to the blade root, maximum-loading region, and blade tip, respectively. Interestingly, at $r/R = 0.30$, the positive thrust condition has a significantly higher periodic variation than the negative thrust condition, see figure 10a. This is in contrast to the fact that the advance ratio varies more significantly in the negative thrust condition, as seen in figure 4. This outcome can be attributed to the reduced sensitivity of the thrust coefficient to the changes in the advance ratio under these conditions, as depicted in the $T_C - J$ curve in refs. [6, 8]. Specifically, the blade section operates at high negative angles of attack, which leads to the formation of a leading-edge separation bubble that reduces the $C_l - \alpha$ slope, consequently reducing the sensitivity of the thrust coefficient to advance ratio variations.

At the outboard sections ($r/R = 0.7$ and 0.9), the relative amplitude of the thrust coefficient is reduced in both conditions due to the corresponding decrease in advance ratio. While broadband fluctuations are negligible in the positive thrust condition at all radial stations, they are noticeable in the negative thrust condition. At $r/R = 0.30$, for instance, broadband fluctuations of up to 7% can be seen between $210° \leq \phi \leq 360°$ in the negative thrust condition. This is attributed to the periodic appearance of the separation bubble, as seen in figures 8e to 8h. Similar behavior can be seen at $r/R = 0.70$ in figure 10b, although with slightly higher intensity (up to 9%).

Surprisingly, at $r/R = 0.90$, the periodic fluctuations are reversed compared to the inboard sections (figure 10c). This is expected to be the consequence of the operation of the blade section in the deep stall region, where the increase of the absolute angle of attack on the retreating side ($180° \leq \phi \leq 360°$) leads to a decreased C_l and the corresponding decreased thrust coefficient. At this radial station, the broadband fluctuations (up to 10%) appear to be almost equally important as the periodic fluctuations (up to 14%).

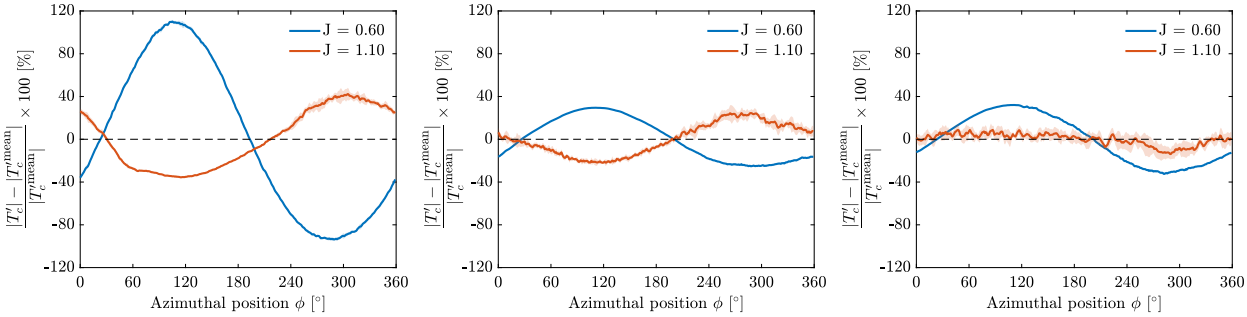

(a) $r/R = 0.30$ **(b)** $r/R = 0.70$ **(c)** $r/R = 0.90$

Fig. 10 Change in the absolute time-averaged thrust coefficient ($|T_c'|$) with respect to the absolute mean value over the azimuthal position (ϕ)

IV. Far-field Aeroacoustic Results

The operation of a propeller at non-zero angles of attack significantly changes the noise characteristics compared to its operation at 0° angle of attack. Two mechanisms account for these changes: the periodic variations in blade

loading and the asymmetric phase modulation of the strength of noise sources. The asymmetric phase modulation is the kinematic/acoustic effect which is a result of the periodic variation of observer-source relative Mach number for an observer rigidly rotating with the blade [32–34]. The present study investigated the relative importance of these two effects by conducting FW-H computations with and without the convective effects due to the freestream cross-flow velocity component ($V_\infty \sin\alpha_\infty$) when operating at the 10° angle of attack (figure 3). The far-field noise was calculated at two planes: the plane of propeller rotation (YZ plane) and the plane along the axis of the propeller (XZ plane). These were computed on two circular arrays of $10D$, centered around the propeller center, with 24 evenly spaced virtual microphones. In both planes, the total noise at the circular arrays was further decomposed into thickness and loading noise using the monopole and dipole terms, respectively, in the so-called solid FW-H formulation [12, 25]. The noise directivity was plotted in terms of Sound Pressure Level (SPL) in two different frequency ranges: $0.9 \leq \text{BPF} \leq 10$ and $0.9 \leq \text{BPF} \leq 1.1$. The former was representative of the overall sound pressure level directivity, whereas the latter was used to investigate the directivity of tonal noise at the most dominant harmonic, i.e., the 1st BPF.

A. Noise Directivity in the Plane of Propeller Rotation

1. Positive thrust condition ($J = 0.60$)

Figure 11 shows the far-field noise directivity in the plane of propeller rotation at the positive thrust condition ($J = 0.60$). Figures 11a and 11b display the noise directivity at 0° and 10° angle of attack, respectively, for the frequency range of $0.9 \leq \text{BPF} \leq 10$. Similarly, Figures 11c and 11d show the noise directivity for the frequency range of $0.9 \leq \text{BPF} \leq 1.1$. In figures 11b and 11d, an additional noise directivity denoted as "Total (no cross-flow)" has been shown with blue-cross markers. This noise directivity has been calculated without the convection effects of the freestream cross-flow velocity component ($V_\infty \sin\alpha_\infty$) and displays the relative importance of the aforementioned asymmetric phase modulation for the given operating condition. The corresponding power spectrum density plots are presented in figure 12.

The noise directivity at 0° angle of attack shows expected axisymmetry around the propeller axis, see figures 11a and 11c. However, when the angle of attack is changed from 0° to 10°, the noise is no longer axisymmetric around the propeller axis (figures 11b and 11d). The total noise is increased in the region from which the propeller is tilted away, i.e., $90° < \phi < 270°$ and decreased in the opposite region, i.e., $270° < \phi \leq 90°$. This is in agreement with the literature [33, 35–37]. The change in the noise directivity is caused by the presence of unsteady (periodic) loading on the propeller blades. Also, the identical results shown by the blue-cross markers confirm that the influence of asymmetric acoustic modulation by the cross-flow velocity component is minor in comparison to the effect of unsteady blade loading for the given case.

The change in the angle of attack from 0° to 10° (figure 6a) results in an increment in noise emissions of up to 5 dB at $\phi = 195°$ and a reduction of up to 7 dB at $\phi = 15°$ in the loading noise. This increase and decrease is a direct result of

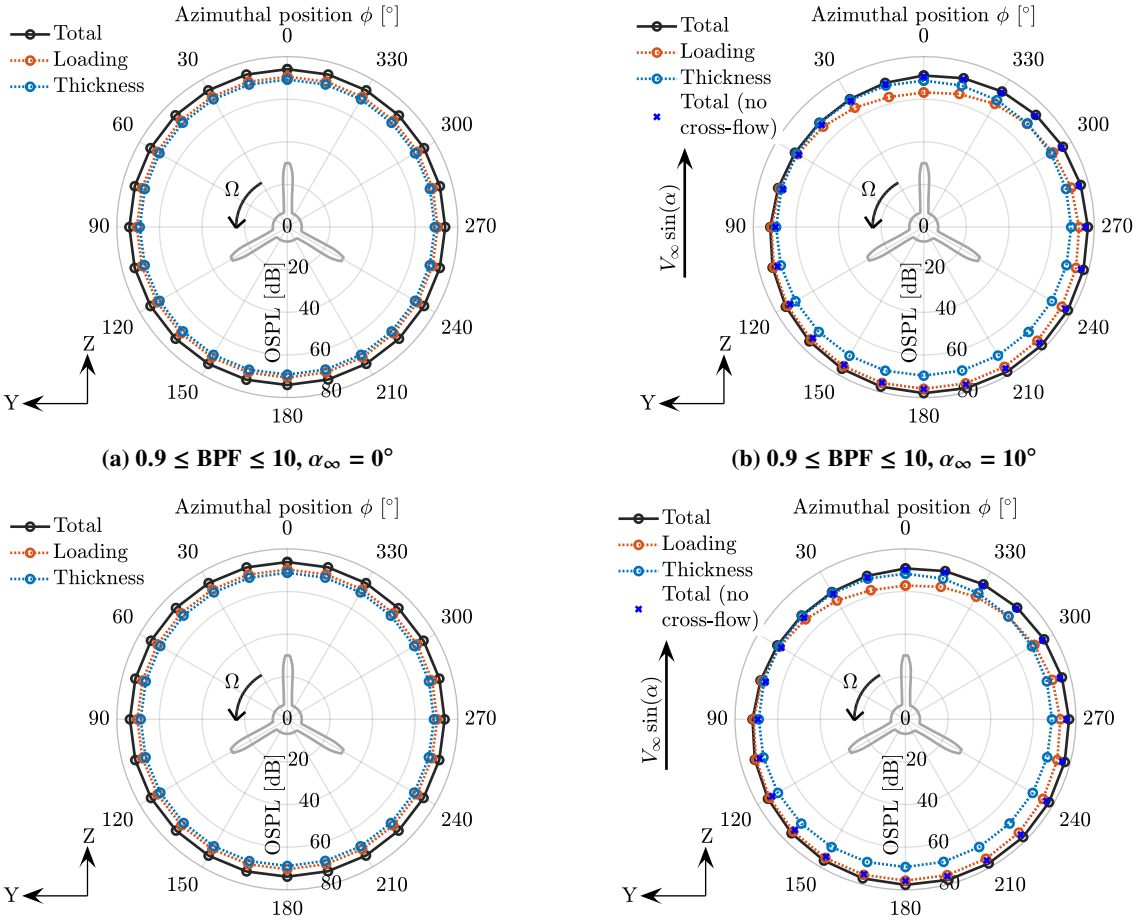

(a) 0.9 ≤ BPF ≤ 10, $\alpha_\infty = 0°$

(b) 0.9 ≤ BPF ≤ 10, $\alpha_\infty = 10°$

(c) 0.9 ≤ BPF ≤ 1.1, $\alpha_\infty = 0°$

(d) 0.9 ≤ BPF ≤ 1.1, $\alpha_\infty = 10°$

Fig. 11 Effect of angle of attack on the azimuthal noise directivity in the plane of rotation at the positive thrust condition ($J = 0.60$)

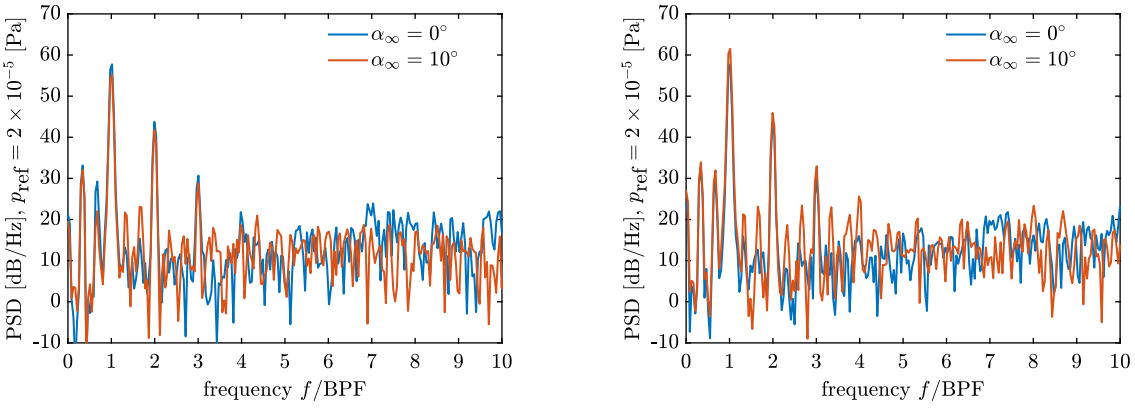

(a) $\phi = 0°$

(b) $\phi = 180°$

Fig. 12 Effect of angle of attack on the power spectrum density in the plane of rotation at the positive thrust condition ($J = 0.60$)

the change in the blade loading at 10° angle of attack compared to 0° angle of attack. Since the loading noise generated by the propeller blades primarily radiates in the perpendicular direction, the maximum and minimum noise locations are located 90° ahead of the maximum and minimum blade loading locations, respectively.

In contrast to the loading noise, the thickness noise exhibits a negligible change (±0.5 dB) with the varying angle of attack. This can be attributed to the relatively smaller variation in the effective velocity at the outboard sections (±3% at the blade tip) compared to the corresponding variation in the blade loading, as previously shown in figure 10. At 0° angle of attack, the thickness noise is almost as significant as the loading noise. However, at the 10° angle of attack, the thickness noise becomes dominant between $300° < \phi < 60°$ due to the decrease in the loading noise, whereas the loading noise remains dominant for the rest of the azimuth.

For further insights into the spectral content of the propeller noise emissions, the power spectrum density (PSD) has been plotted in figure 12. The PSD is presented for two azimuthal positions, 0° and 180°, which correspond to the regions of maximum decrease and increase of the loading noise, respectively. At 10° angle of attack, a decrease is observed in the first BPF at $\phi = 0°$ and an increase at $\phi = 180°$, which is consistent with the noise directivity plots. Similar trends can be observed for the 2nd and 3rd BPFs. Additionally, at $\phi = 0°$, the decrease in the tonal harmonics is also accompanied by a decrease in the broadband noise between 7-10 BPFs, as shown in figure 12a. However, this cannot be said for the PSD at $\phi = 180°$, as shown in figure 12b.

2. Negative thrust condition ($J = 1.10$)

The noise directivity plots for the negative thrust condition ($J = 1.10$) are shown in figure 13. Similar to the positive thrust case ($J = 0.60$) at 0° angle of attack, an axisymmetric trend is observed. However, unlike the positive thrust case, the thickness noise is no longer the dominant noise source. This is because the reduced tip Mach number at $J = 1.10$ compared to $J = 0.60$ results in a decrease in the thickness noise, which is more sensitive to the tip Mach number than the loading noise. Additionally, the loading noise is significantly reduced in the negative thrust condition compared to the positive thrust condition. This is due to the lower magnitude of T_C (Table 2) as well as the inboard shift of the loading [6] in the negative thrust case.

Similar to $J = 0.60$, the blue-cross markers in figure 13b and 13d represent the change in the noise without considering the convection effect of the cross-flow component. The blue-cross markers show similar results as the total noise with the cross-flow component (figure 13b) indicating that the change in the noise directivity is again dominated by the unsteady blade loading. Figure 13b shows that the noise is increased by up to 4 dB between $270° \leq \phi \leq 90°$ and only marginally for the other part at 10° angle of attack compared to 0°. This trend seems to be in contrast with the positive thrust condition (figure 11b), where a decrease was observed between $270° \leq \phi \leq 90°$ and an increase between $90° \leq \phi \leq 270°$. This change in noise directivity is driven by two factors. One is the change in the tonal noise directivity at propeller harmonics, and the second is the change in the broadband noise. These effects are explained in

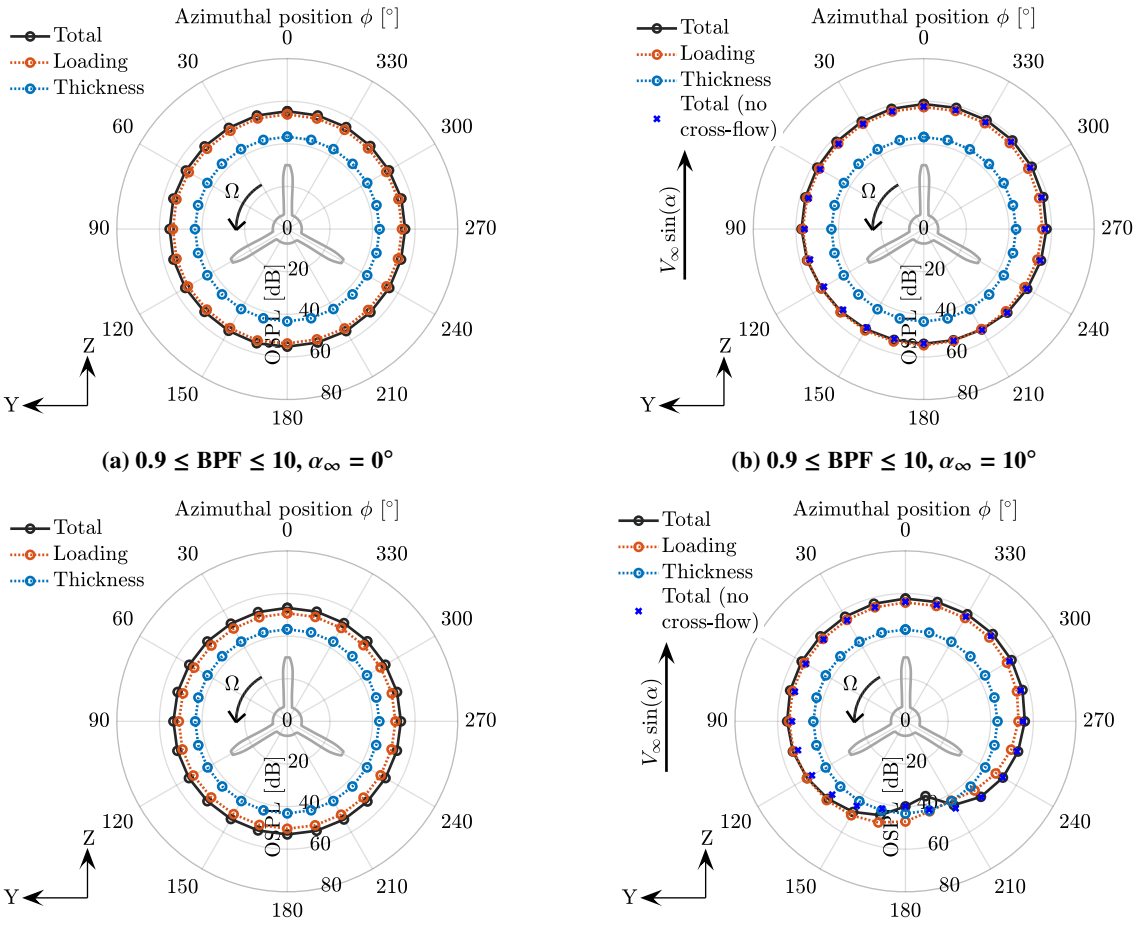

(a) 0.9 ≤ BPF ≤ 10, α_∞ = 0°

(b) 0.9 ≤ BPF ≤ 10, α_∞ = 10°

(c) 0.9 ≤ BPF ≤ 1.1, α_∞ = 0°

(d) 0.9 ≤ BPF ≤ 1.1, α_∞ = 10°

Fig. 13 Effect of angle of attack on the azimuthal noise directivity in the plane of rotation at the negative thrust condition (J = 1.10)

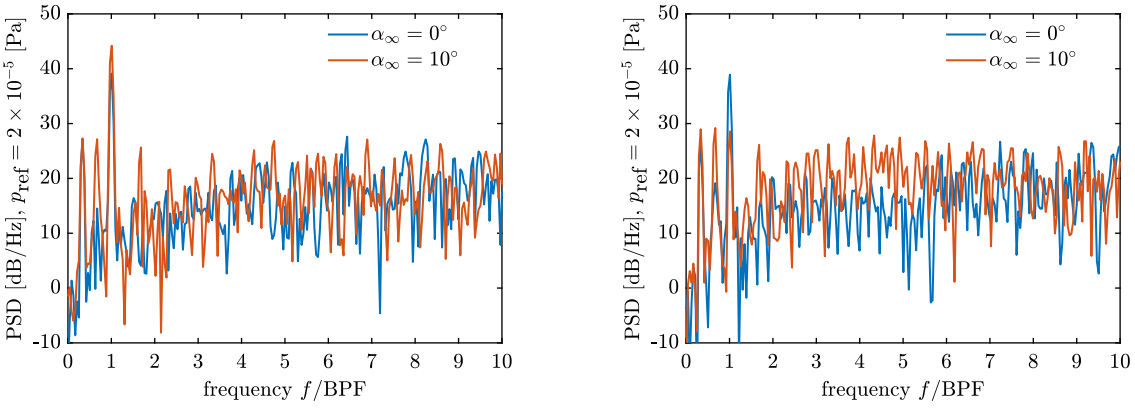

(a) ϕ = 0°

(b) ϕ = 180°

Fig. 14 Effect of angle of attack on the power spectrum density in the plane of rotation at the negative thrust condition (J = 1.10)

the following paragraphs.

Figure 13d shows the noise directivity of the first harmonic at 10° angle of attack. It shows a decrease of up to 8 dB in the region from which the propeller is tilted away ($90° < \phi < 270°$) and an increment of up to 5 dB in the opposite direction ($0° \leq \phi < 90°$ and $270° < \phi \leq 0°$) as compared to 0° angle of attack (figure 13c). As mentioned before, this is opposite to the trend observed for the positive thrust condition ($J = 0.60$). This can be explained by revisiting the changes in blade loading shown in figure 6. As the variation in the absolute blade loading in the negative thrust condition is 180° out of phase as compared to the positive thrust condition, the corresponding changes in the loading noise directivity are also out of phase by 180°. Surprisingly for this operating condition, the interference between the thickness and the loading noise becomes destructive between $120° < \phi < 210°$ resulting in decreased tonal noise. This effect is also observable in figure 13b, where the total noise level is slightly lower than the loading noise levels between the aforementioned azimuthal positions.

The relative level of tonal and broadband noise can be observed by examining the PSD at two azimuthal positions: $\phi = 0°$ and $\phi = 180°$, as shown in figure 14. Figure 14a depicts an increase in the noise at the first BPF at $\alpha_\infty = 10°$, consistent with the results presented in figure 13d. Furthermore, the broadband noise levels are comparable at both α_∞ values. At $\phi = 180°$, the noise level at the first BPF is significantly reduced. However, there is a considerable increase in broadband noise, which compensates for the decrease of the tonal noise at the first BPF. This increase in broadband noise is expected to originate from the stalling of the blade tip, as seen in figure 10c. Consequently, the noise levels are almost the same or even higher between $90° < \phi < 270°$ between the two angles of attack as depicted in figure 13b.

B. Noise Directivity in the Plane along the Propeller Axis

1. Positive thrust condition ($J = 0.60$)

Figure 15 illustrates the noise directivity along the propeller axis for the positive thrust condition ($J = 0.60$). As thickness noise is a tonal noise source, it mainly radiates in the propeller plane (69 dB) and has zero contribution along the propeller axis, as seen in figure 15a. On the other hand, the loading noise has both broadband and tonal noise components, leading to a noise level of 61 dB along the propeller axis and 71 dB in the propeller plane. This is also evident from figure 15c, where the tonal noise from the first harmonic mainly propagates in the propeller plane, resulting in a total noise level of 74 dB at $\theta = 90°$, compared to the noise level of 32 dB along the propeller axis ($\theta = 0°$).

While the noise directivity is symmetric around the propeller axis at 0° angle of attack (as expected), the same is not true at the 10° angle of attack. For the positive thrust condition, the OSPL is increased in the region where the propeller is tilted away and vice versa, as shown in figure 15a, which agrees with the trends seen in section IV.A.1. The change in the noise directivity is mainly driven by changes in the loading noise at the 1st BPF, as observed in figures 15b and 15d. The maximum change in the total noise is up to ±8 dB at $\theta = 210°$ and 135°, respectively, due to the significant decrease in the loading noise. As a result, the thickness noise becomes the dominant source of noise between $75 \leq \theta \leq 135°$.

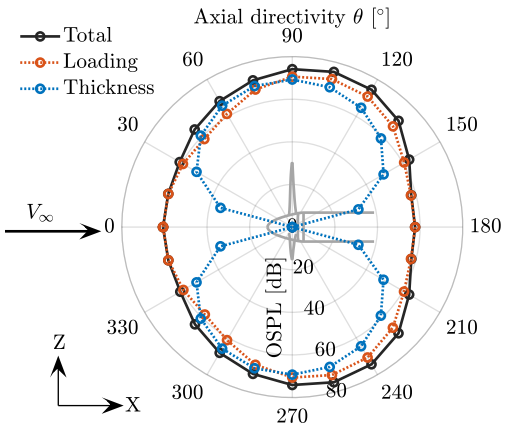

(a) $0.9 \leq \text{BPF} \leq 10$, $\alpha_\infty = 0°$

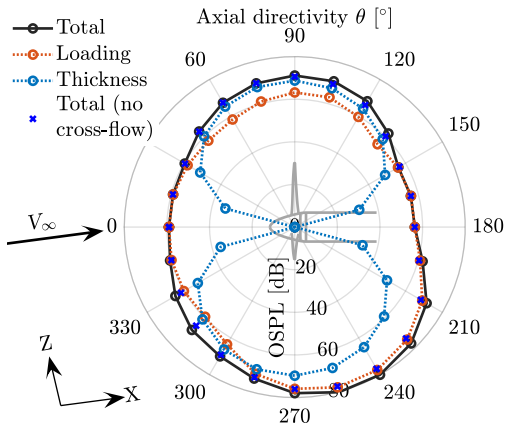

(b) $0.9 \leq \text{BPF} \leq 10$, $\alpha_\infty = 10°$

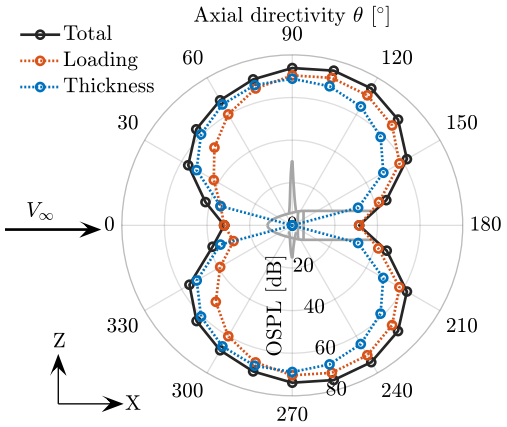

(c) $0.9 \leq \text{BPF} \leq 1.1$, $\alpha_\infty = 0°$

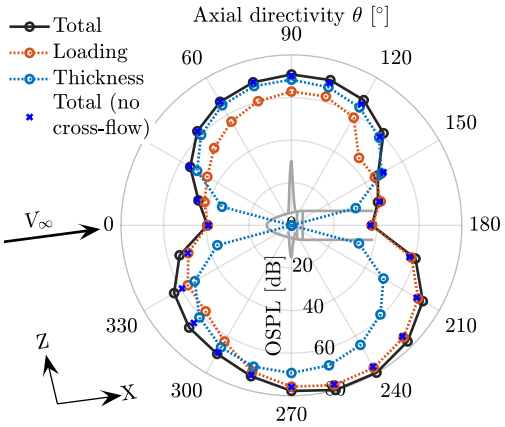

(d) $0.9 \leq \text{BPF} \leq 1.1$, $\alpha_\infty = 10°$

Fig. 15 Effect of angle of attack on the noise directivity along the propeller axis at the positive thrust condition ($J = 0.60$)

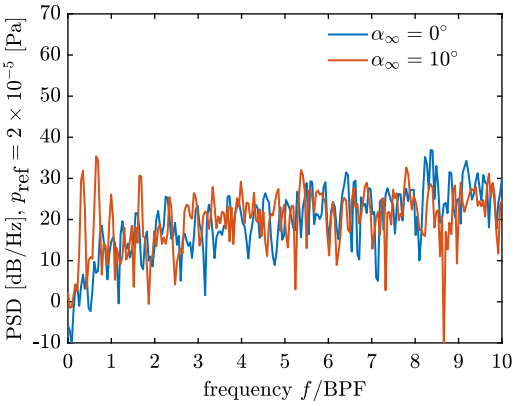

(a) $\theta = 0°$ (upstream)

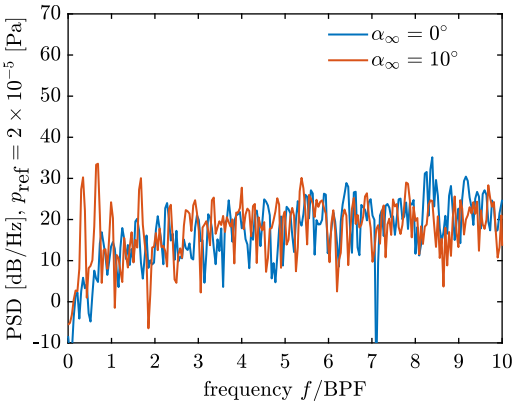

(b) $\theta = 180°$ (downstream)

Fig. 16 Effect of angle of attack on the power spectrum density along the propeller axis at the positive thrust condition ($J = 0.60$)

Although the tonal noise changes significantly with the angle of attack, the broadband noise remains almost constant. This can be observed from the PSD plots shown in figure 16. These plots show that there is no tonal noise at 0° angle of attack, but tonal peaks appear at $\alpha_\infty = 10°$, albeit small. Therefore, contrary to the noise associated with steady blade loading at 0° angle of attack, unsteady blade loading leads to the propagation of noise along the propeller axis, which is in agreement with the literature [28, 34].

Similar to the previous section IV.A.1, the noise without the convective effect of the cross-flow velocity component (blue-cross markers) shows similar trends as the noise with the convective effect of the cross-flow velocity (figures 15b and 15d). Therefore, the asymmetric modulation of the noise sources is also irrelevant in the plane perpendicular to the plane of rotation.

2. Negative thrust condition ($J = 1.10$)

Figure 17 shows the noise directivity in the plane aligned with the propeller axis for the negative thrust condition ($J = 1.10$). As previously mentioned in section IV.A.2, the thickness noise is significantly reduced at $J = 1.10$ compared to $J = 0.60$, making the loading noise the dominant source of noise at both 0° and 10° angle of attack. The loading noise is higher along the propeller axis (64 dB at $\theta = 0°$ and 62 dB at 180°) than in the propeller plane (54 dB at $\theta = 90°$ and 270°), as shown in figure 17a, indicating the presence of high broadband noise in the negative thrust condition. The high broadband noise is a result of the flow separation around the propeller blades. The reduced tonal noise compared to the positive thrust condition is partially due to the reduced absolute loading and reduced tip Mach number but also due to the change in the loading distribution along the blade span. Again, the noise directivity at 0° angle of attack is symmetric around the propeller axis as expected.

The directivity of noise at the 1st harmonic at 0° angle of attack (figure 17c) shows a significant noise along the propeller axis (40 dB), indicating the presence of broadband noise between $0.9 \leq BPF \leq 1.1$, as can also be seen in the PSD plots in figure 18. Interestingly, the directivity at the 1st BPF shows that there is destructive interference between loading and thickness noise at $0° < \theta < 75°$, resulting in lower total noise at these axial directivity angles.

At the 10° angle of attack, the directivity of noise is significantly altered with respect to the 0°, as can be seen in figure 17. The loading noise is increased up to 4.5 dB between $90° <\leq \theta \leq 180°$ and reduced up to 4 dB between $180° <\leq \theta \leq 270°$ compared to 0° angle of attack, as shown in figure 17b. These changes in the noise levels are again opposite to the trends seen for $J = 0.60$. As explained before in section IV.A.2, the opposite changes in the noise directivity at non-zero angles of attack are the consequence of opposite changes in the absolute blade loading over the advancing and retreating sides of the rotation (figure 10). The blue-cross markers, like all the previous results, show identical results, indicating that the dominant mechanism responsible for changes in noise directivity at the 10° angle of attack is unsteady loading.

The directivity of loading noise at the first BPF (figure 17d) also shows similar changes with the change in the angle

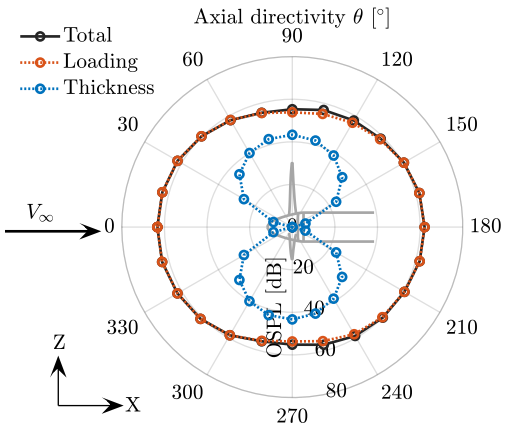

(a) 0.9 ≤ BPF ≤ 10, α_∞ = 0°

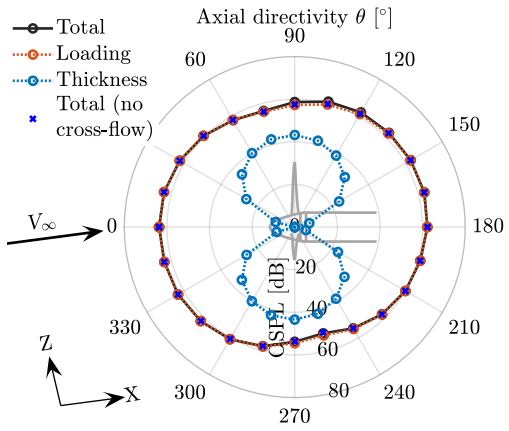

(b) 0.9 ≤ BPF ≤ 10, α_∞ = 10°

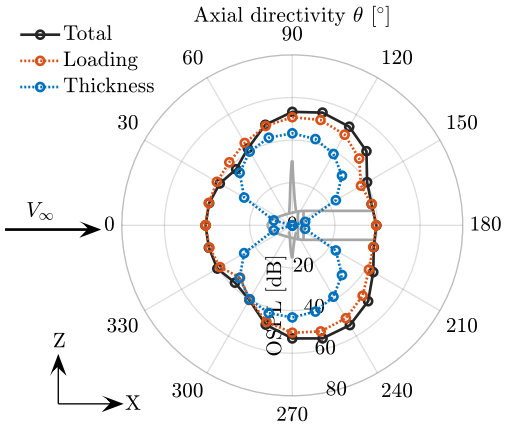

(c) 0.9 ≤ BPF ≤ 1.1, α_∞ = 0°

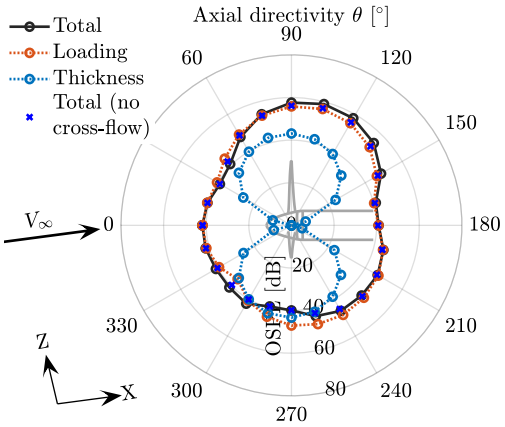

(d) 0.9 ≤ BPF ≤ 1.1, α_∞ = 10°

Fig. 17 Effect of angle of attack on the noise directivity along the propeller axis at the negative thrust condition (J = 1.10)

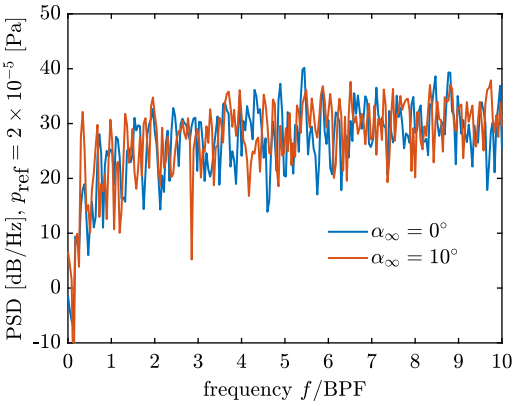

(a) θ = 0° (upstream)

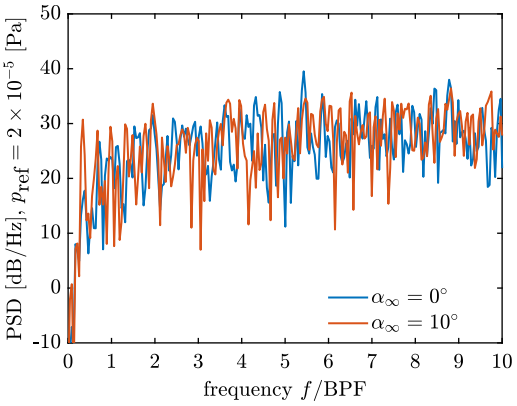

(b) θ = 180° (downstream)

Fig. 18 Effect of angle of attack on the power spectrum density along the propeller axis at the negative thrust condition (J = 1.10)

of attack. However, an interesting change can be seen in the interference of the loading and thickness noise. In addition to the observed destructive interference between loading and thickness noise for $0° < \theta < 75°$ at 0° angle of attack, there is also destructive interference for $210° \leq \theta < 300°$ at 10° angle of attack. This destructive interference leads to reduced total noise in the lower part of the plane.

Contrary to expectations, the broadband noise stays almost constant with the change of angle of attack. This can be also seen from PSD plots shown in figure 16. Additionally, the plots indicate that there is no tonal noise at 0° angle of attack, but small tonal peaks appear at $\alpha_\infty = 10°$, leading to a slight increase in noise along the propeller axis, similar to the positive thrust condition.

V. Conclusions

In this paper, the effect of the non-zero angle of attack on the aeroacoustic performance of a conventional propeller has been quantified and explained when operating in both positive and negative thrust conditions. The following conclusions are drawn by comparing the aerodynamic performance of the propeller at 0° and 10° angle of attack:

- Due to the change in effective advance ratio, the thrust and torque increase on the advancing side and decrease on the retreating side in the positive thrust condition ($J = 0.60$), resulting in an overall 9.6% increase in thrust and 5.5% increase in power. Since the increase in thrust is greater than the increase in power, the propeller efficiency along the propeller axis is improved by 3.8%.
- In contrast to the positive thrust condition, the negative thrust condition ($J = 1.10$) shows a decrease in the thrust magnitude on the advancing side and an increase on the retreating side. This results in an overall 7.9% decrease in the integrated thrust and an 11.1% decrease in the power magnitude. Consequently, both turbine and energy-harvesting efficiencies are reduced.
- At a non-zero angle of attack, the positive thrust condition shows a decrease in the absolute thrust acting along the freestream direction when compared to the propeller axis. However, due to the contribution of the normal force, absolute thrust is higher along the freestream direction in the negative thrust condition.
- The difference between the torque on the advancing and retreating sides of the propeller generates an in-plane force that can be split into two components: normal force and side force. Although the direction of thrust and torque is reversed between positive and negative thrust regimes, the direction of normal and side force remains unaffected.
- At a non-zero angle of attack, the positive thrust condition results in a perpendicular force (lift force) due to the positive contributions from the thrust and normal forces along the propeller axis. Conversely, the negative thrust condition produces a negative lift force due to the reversed direction of thrust. However, the magnitude of the negative lift force is decreased due to the negative contribution from the normal force.
- The inboard blade sections start to exhibit dynamic stall at 10° angle of attack due to the attachment of the flow on the advancing side and the separation of the retreating side in the negative thrust condition. As the outboard blade

sections are already stalled in the uniform inflow case, only the extent of separation is changed over the rotation.

- In the negative thrust condition, the outboard part of the blade exhibits significant broadband fluctuations, even at a 0° angle of attack. These fluctuations can reach up to 10% of the mean loading and are almost as strong as the periodic variations (up to 14% of the mean loading) observed at a 10° angle of attack. Moreover, at the 10° angle of attack, the broadband fluctuations decrease on the advancing side of the blade and increase on the retreating side.

The changes in the propeller blade loading lead to changes in the far-field aeroacoustic performance. These noise changes were investigated in two planes: the plane of propeller rotation and the plane along the propeller axis. The following conclusions are drawn regarding the changes in the far-field noise emissions:

- In both positive and negative thrust conditions investigated in this paper, the unsteady loading is the driving mechanism for the change in the noise directivity with the change in the angle of attack. The asymmetric modulation of the noise sources due to the cross-flow component has negligible impact due to the low tip-Mach number of the cases considered. This might change for a more realistic case.
- The loading noise directivity in both the plane of rotation and the plane perpendicular to the plane of rotation is affected differently by the angle of attack in positive and negative thrust conditions. In the positive thrust condition, the loading noise is increased in the region from which the propeller is tilted away and decreased in the region from which it is tilted towards. On the other hand, the opposite trend is observed in the negative thrust condition, where the loading noise is decreased in the region from which the propeller is titled away and increased in the region from which it is tilted towards. These opposite trends are due to the opposite changes in the absolute blade loading caused by the angle of attack.
- The noise levels along the propeller axis are higher than those in the propeller plane in the negative thrust condition, which is in contrast to the positive thrust condition.
- At the negative thrust condition, the thickness noise and loading noise interfere destructively at certain azimuthal and axial positions, resulting in reduced total noise at those locations. However, the exact cause of this interference is not fully understood and requires further investigation. In contrast, this phenomenon is not observed in the positive thrust condition.

The novel results presented in this paper provide valuable insights into the aerodynamic and aeroacoustic behavior of conventional propellers operating in negative thrust conditions. This is an important step towards enhancing the understanding of the complex propeller-wing interactions that occur under such conditions.

Acknowledgments

The research leading to these results is part of the FUTPRINT50 project. This project has received funding from the European Union's Horizon 2020 Research and Innovation programme under Grant Agreement No 875551. This work

made use of the Dutch national e-infrastructure with the support of the SURF Cooperative using grant no. EINF-2733. The authors would like to thank Robert Nederlof for providing the experimental data for the validation of the simulations.

References

[1] Veldhuis, L. L. M., *Propeller wing aerodynamic interference*, Ph.D. Dissertation, Delft University of Technology, Netherlands, 2005. URL http://resolver.tudelft.nl/uuid:8ffbde9c-b483-40de-90e0-97095202fbe3.

[2] Hartman, E. P., "Negative Thrust and Torque Characteristics of an Adjustable-pitch Metal Propeller," *Annual Report-National Advisory Committee for Aeronautics*, Vol. 19, 1933, p. 421. URL http://hdl.handle.net/2060/19930091538.

[3] Hedrick, W. S., and Douglass, W. M., "An Experimental Investigation of the Thrust and Torque Produced by Propellers Used as Aerodynamic Brakes," Tech. Rep. NACA-WR-A-27, National Advisory Committee for Aeronautics, 1944. URL http://hdl.handle.net/2060/19930093338.

[4] Thomas, J. L., and Hansman, R. J., "Community Noise Reduction Assessment of Using Windmilling Drag on Approach by Hybrid Electric Aircraft," *AIAA Aviation 2020 Forum*, AIAA Paper 2020-2877, June 2020. https://doi.org/10.2514/6.2020-2877.

[5] Eržen, D., Andrejašič, M., Lapuh, R., Tomažič, J., Gorup, Č., and Kosel, T., "An Optimal Propeller Design for In-Flight Power Recuperation on an Electric Aircraft," *2018 Aviation Technology, Integration, and Operations Conference*, AIAA Paper 2018-3206, June 2018. https://doi.org/10.2514/6.2018-3206.

[6] Goyal, J., Sinnige, T., Avallone, F., and Ferreira, C., "Aerodynamic and Aeroacoustic Characteristics of an Isolated Propeller at Positive and Negative Thrust," *AIAA Aviation 2021 Forum*, AIAA Paper 2021-2187, June 2021. https://doi.org/10.2514/6.2021-2187.

[7] Nederlof, R., Ragni, D., and Sinnige, T., "Experimental Investigation of the Aerodynamic Performance of a Propeller at Positive and Negative Thrust and Power," *AIAA AVIATION 2022 Forum*, AIAA Paper 2022-3893, June 2022. https://doi.org/10.2514/6.2022-3893.

[8] Sinnige, T., Stokkermans, T. C. A., van Arnhem, N., and Veldhuis, L. L. M., "Aerodynamic Performance of a Wingtip-Mounted Tractor Propeller Configuration in Windmilling and Energy-Harvesting Conditions," *AIAA Aviation 2019 Forum*, AIAA Paper 2019-3033, June 2019. https://doi.org/10.2514/6.2019-3033.

[9] van Arnhem, N., "Unconventional Propeller-Airframe Integration for Transport Aircraft Configurations," 2022. https://doi.org/10.4233/uuid:4d47b0db-1e6a-4f38-af95-aafd33c29402.

[10] Bres, G., Pérot, F., and Freed, D., "Properties of the lattice Boltzmann method for acoustics," *15th AIAA/CEAS Aeroacoustics Conference (30th AIAA Aeroacoustics Conference)*, 2009, p. 3395. https://doi.org/10.2514/6.2009-3395.

[11] Marié, S., Ricot, D., and Sagaut, P., "Comparison between lattice Boltzmann method and Navier–Stokes high order schemes for computational aeroacoustics," *Journal of Computational Physics*, Vol. 228, No. 4, 2009, pp. 1056–1070. https://doi.org/10.1016/j.jcp.2008.10.021.

[12] Farassat, F., and Succi, G. P., "A review of propeller discrete frequency noise prediction technology with emphasis on two current methods for time domain calculations," *Journal of Sound and Vibration*, Vol. 71, No. 3, 1980, pp. 399–419. https://doi.org/10.1016/0022-460X(80)90422-8.

[13] Casalino, D., Hazir, A., and Mann, A., "Turbofan broadband noise prediction using the Lattice Boltzmann Method," *AIAA Journal*, Vol. 56, No. 2, 2018, pp. 609–628. https://doi.org/10.2514/1.J055674.

[14] Gonzalez-Martino, I., and Casalino, D., "Fan tonal and broadband noise simulations at transonic operating conditions using lattice-Boltzmann methods," *2018 AIAA/CEAS Aeroacoustics Conference*, 2018, p. 3919. https://doi.org/10.2514/6.2018-3919.

[15] Succi, S., *The lattice Boltzmann equation: for fluid dynamics and beyond*, Oxford university press, 2001. https://doi.org/10.1063/1.1537916.

[16] Shan, X., Yuan, X.-F., and Chen, H., "Kinetic theory representation of hydrodynamics: a way beyond the Navier–Stokes equation," *Journal of Fluid Mechanics*, Vol. 550, 2006, pp. 413–441. https://doi.org/10.1017/S0022112005008153.

[17] Casalino, D., Romani, G., Zhang, R., and Chen, H., "Lattice-Boltzmann calculations of rotor aeroacoustics in transitional boundary layer regime," *Aerospace Science and Technology*, Vol. 130, 2022, p. 107953. https://doi.org/10.1016/j.ast.2022.107953.

[18] Romani, G., Grande, E., Avallone, F., Ragni, D., and Casalino, D., "Performance and noise prediction of low-Reynolds number propellers using the Lattice-Boltzmann method," *Aerospace Science and Technology*, Vol. 125, 2022, p. 107086. https://doi.org/10.1016/j.ast.2021.107086, sI: DICUAM 2021.

[19] Casalino, D., Grande, E., Romani, G., Ragni, D., and Avallone, F., "Definition of a benchmark for low Reynolds number propeller aeroacoustics," *Aerospace Science and Technology*, Vol. 113, 2021, p. 106707. https://doi.org/10.1016/j.ast.2021.106707.

[20] Chen, H., Zhang, R., and Gopalakrishnan, P., "Lattice Boltzmann collision operators enforcing isotropy and Galilean invariance," , Feb. 21 2017. URL https://patents.google.com/patent/CA2919062A1/en.

[21] Chen, H., Chen, S., and Matthaeus, W. H., "Recovery of the Navier-Stokes equations using a lattice-gas Boltzmann method," *Physical review A*, Vol. 45, No. 8, 1992, p. R5339. https://doi.org/10.1103/PhysRevA.45.R5339.

[22] Yakhot, V., and Orszag, S. A., "Renormalization group analysis of turbulence. I. Basic theory," *Journal of scientific computing*, Vol. 1, No. 1, 1986, pp. 3–51. https://doi.org/10.1007/BF01061452.

[23] Teixeira, C. M., "Incorporating turbulence models into the lattice-Boltzmann method," *International Journal of Modern Physics C*, Vol. 9, No. 08, 1998, pp. 1159–1175. https://doi.org/10.1142/S0129183198001060.

[24] Wilcox, D. C., "Turbulence Modelling for CFD 3rd Edition," *La Canada CA: DCW industries*, 2006.

[25] Casalino, D., "An advanced time approach for acoustic analogy predictions," *Journal of Sound and Vibration*, Vol. 261, No. 4, 2003, pp. 583–612. https://doi.org/10.1016/S0022-460X(02)00986-0.

[26] Kurtz, D., and Marte, J., "A review of aerodynamic noise from propellers, rotors, and lift fans," Tech. Rep. 32-1462, Jet Propulsion Laboratory, Jan. 1970. URL https://ntrs.nasa.gov/citations/19700005920.

[27] Avallone, F., van den Ende, L., Li, Q., Ragni, D., Casalino, D., Eitelberg, G., and Veldhuis, L., "Aerodynamic and Aeroacoustic Effects of Swirl Recovery Vanes Length," *Journal of Aircraft*, Vol. 56, No. 6, 2019, pp. 2223–2235. https://doi.org/10.2514/1.C035552.

[28] Romani, G., Grande, E., Avallone, F., Ragni, D., and Casalino, D., "Computational study of flow incidence effects on the aeroacoustics of low blade-tip Mach number propellers," *Aerospace Science and Technology*, Vol. 120, 2022, p. 107275. https://doi.org/10.1016/j.ast.2021.107275.

[29] van Arnhem, N., Vos, R., and Veldhuis, L. L. M., "Aerodynamic Loads on an Aft-Mounted Propeller Induced by the Wing Wake," *AIAA Scitech 2019 Forum*, AIAA Paper 2019-1093, Jan. 2019. https://doi.org/10.2514/6.2019-1093.

[30] De Young, J., "Propeller at high incidence," *Journal of Aircraft*, Vol. 2, No. 3, 1965, pp. 241–250. https://doi.org/10.2514/3.43646.

[31] Ortun, B., Boisard, R., and Gonzalez-Martino, I., "In-plane airloads of a propeller with inflow angle: prediction vs. experiment," *30th AIAA Applied Aerodynamics Conference*, 2012, p. 2778. https://doi.org/10.2514/6.2012-2778.

[32] Carley, M., "The structure of wobbling sound fields," *Journal of sound and vibration*, Vol. 244, No. 1, 2001, pp. 1–19. https://doi.org/10.1006/jsvi.2000.3451.

[33] Mani, R., "The radiation of sound from a propeller at angle of attack," *Proceedings of the Royal Society of London. Series A: Mathematical and Physical Sciences*, Vol. 431, No. 1882, 1990, pp. 203–218. https://doi.org/10.1098/rspa.1990.0127.

[34] Hanson, D., "Sound from a propeller at angle of attack: a new theoretical viewpoint," *Proceedings of the Royal Society of London. Series A: Mathematical and Physical Sciences*, Vol. 449, No. 1936, 1995, pp. 315–328. https://doi.org/10.1098/rspa.1995.0046.

[35] Block, P., "The effects of installation on single-and counter-rotation propeller noise," *9th Aeroacoustics Conference*, 1984, p. 2263. https://doi.org/10.2514/6.1984-2263.

[36] Block, P., *Experimental study of the effects of installation on single-and counter-rotation propeller noise*, Vol. 2541, National Aeronautics and Space Administration, Scientific and Technical Information Branch, 1986. URL https://ntrs.nasa.gov/citations/19860016690.

[37] Woodward, R., "Measured noise of a scale model high speed propeller at simulated takeoff/approach conditions," *25th AIAA Aerospace Sciences Meeting*, 1987, p. 526. URL https://ntrs.nasa.gov/citations/19870043835.